Modeling Surface Multipath Effects in Synthetic Aperture Sonar

Brynmor J. Davis, *Member, IEEE*, Peter T. Gough, *Senior Member, IEEE*, and Bobby R. Hunt, *Life Fellow, IEEE*

***Abstract*—Synthetic aperture sonar (SAS) imaging algorithms assume a specific ping-to-ping phase relation in the collected data. The line-of-sight signal from a nonmoving object adds coherently from ping to ping in the image reconstruction process while any random multipath reflections or backscatter from the sea surface may add noncoherently, thus improving the image signal-to-clutter ratio (SCR). To move towards understanding just how effective a SAS is at suppressing surface multipath contributions, it is necessary to model the moving surface in a believable way and establish how the sound reflects from the undersurface of the sea. This paper presents a method for simulating the effects of multipath propagation on sonar data and hence evaluating the SCR improvement realized with synthetic aperture processing. This paper first reviews the Pierson–Moskowitz and cos-2s surface-wave spectra, which together account for wind direction, wind speed, and angular spread of the wave propagation direction. From these spectra a statistically appropriate random wave surface is generated which evolves in both time and space. In a first attempt to model the sea-surface multipath problem, a set of impulse responses are generated from this wave surface as it evolves in time increments equal to the pulse repetition period. Two sea-surface scattering mechanisms are used in the simulations described in this paper. In the first, each surface facet reflects as a diffraction-limited radiating aperture and in the second, each facet reflects as an incoherent Lambertian scatterer. These describe two limiting situations: first, the acoustic wavelength is small compared with the roughness of the sea surface; and second, the acoustic wavelength is significant in proportion to the surface roughness. The effect of surface multipath is shown on raw data and also on processed SAS images. The calculation of the SCR as a function of sea state is also demonstrated. The SCR improvement seen with SAS imaging is consistent with the hypothesis that surface multipath signals are fully incoherent from ping to ping.**

***Index Terms*—Clutter, image reconstruction, surface multipath, synthetic aperture sonar.**

I. Introduction

THE imaging fidelity of any standard side looking sonar is degraded by sea-surface multipath reflections and seafloor multipath reflections, as shown in Fig. 1. Since the objects of interest are often either buried or in close proximity to the seafloor, seafloor multipath is inextricably linked to the direct backscatter of the object and it stays reasonably constant with time although it does vary with the azimuthal angle of incidence. Sea-surface backscatter and multipath are different in that they change quite rapidly with time. By using synthetic aperture sonar (SAS) techniques, the random nature of the sea-surface multipath returns can be exploited.

All SAS systems record the pulse echo returns in both amplitude and phase so they can, by using coherent integration, compute an image from a contiguous collection of ping echoes as if it came from a much larger physical aperture [1]. For SAS to work there are some critical assumptions. The first is that the platform moves in a predictable and usually linear track. A combination of highly accurate navigation units and autofocus techniques (sometimes called micronavigation) can now correct the problems caused by nonlinear track [2], [3]. The second assumption, and the one pertinent to this paper, is that the phase of a collected echo is determined by the line-of-sight distance from the reflector to the prescribed sonar position. Since multipath echoes traverse a different path to the receiver, this assumption is violated. It is important to establish how this affects the data collected and more importantly how it affects the final image.

To do this, the complete sonar data collection and imaging system is simulated, both with and without the sea-surface effects. A statistical model is used to produce sea-surface height functions and scattering is calculated from these. A facet-ensemble approach [4]–[7] is used to calculate the signal return from the sea surface. Unfortunately, if all the multipath effects are included in the simulation, the model becomes extremely complicated, so attention is restricted to only the effects of sea-surface multipath on the reflected echoes. That is, it is assumed that the vertical beamwidth of the projector is small enough to eliminate any sea-surface backscatter or multipath on the outward leg of the acoustic path and that there are no seafloor multipath effects. It should be noted that in certain imaging conditions the sea-floor effects can be significant [8].

II. Generating Sea-Surface Displacement Functions

In order to simulate the multipath returns from the sea surface, it is necessary to have a time-evolving model of the sea surface. Here a stochastic approach is used as it captures the nondeterministic nature of the sea surface. Specifically, the Pierson–Moskowitz spectrum [9], the cos-2s directional spectrum [10], and the dispersion relation [11] are used to define a spatio–temporal random process that represents sea-surface displacement.

Manuscript received March 08, 2007; revised September 12, 2007 and October 19, 2008; accepted January 25, 2009. Current version published August 05, 2009.

Guest Editor: P. E. Hagen.

B. J. Davis was with the University of Arizona, Tucson, AZ 85721 USA. He is now with the Beckman Institute for Advanced Science and Technology, University of Illinois at Urbana-Champaign, Urbana, IL 61801 USA (e-mail: bryn_davis@hotmail.com; bryn@uiuc.edu).

P. T. Gough is with the Electrical and Computer Engineering Department, University of Canterbury, Christchurch 8140, New Zealand (e-mail: gough@elec.canterbury.ac.nz; peter.gough@canterbury.ac.nz).

B. R. Hunt is with the University of Arizona, Tucson, AZ 85721 USA and the University of Canterbury, Christchurch 8140, New Zealand (e-mail: brhunt@brhunt.com).

Digital Object Identifier 10.1109/JOE.2009.2017796

0364-9059/$26.00 © 2009 IEEE

Authorized licensed use limited to: University of Illinois. Downloaded on August 5, 2009 at 17:03 from IEEE Xplore. Restrictions apply.

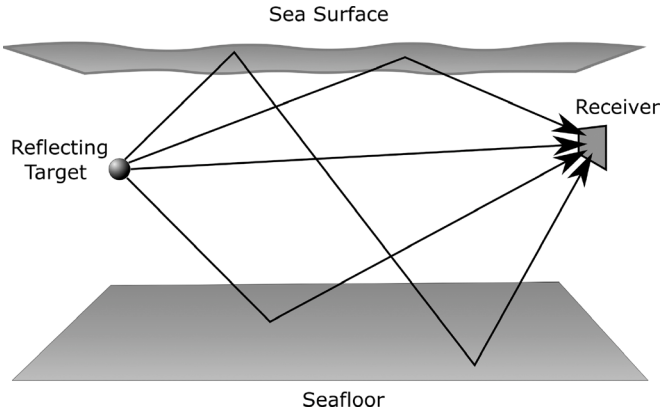

Fig. 1. Illustration of multipath propagation due to sea-surface and seafloor reflections.

The Pierson–Moskowitz model of the temporal spectrum of a fully developed sea is

$$P(\omega) = \frac{0.0081g^2}{\omega^5} \exp\left[-0.74\left(\frac{g}{W\omega}\right)^4\right] \tag{1}$$

where ω is the angular frequency of the wave, g is gravitational acceleration, and W is the wind speed 19.5 m above the sea surface.

A directional spectrum is used to model the dependence of the wave spectrum on ξ, the angle from the principal wave direction. The cos-2s angular dependence is

$$D(\xi) = \frac{\Gamma(s+1)}{2\sqrt{\pi}\Gamma\left(s+\frac{1}{2}\right)} \cos^{2s}\left(\frac{\xi}{2}\right), \qquad s > 0. \tag{2}$$

The parameter s is chosen to give the desired angular width, ξ ranges between $-\pi$ and π, and $\Gamma(\cdot)$ is the gamma function.

The temporal frequencies of the waves are related to the spatial frequencies through the dispersion relation

$$\omega^2 = g\sqrt{k_w^2 + k_c^2}\tanh\left(\sqrt{k_w^2 + k_c^2}d\right) \tag{3}$$

where k_w and k_c are windward and crosswind spatial wave numbers and the variable d is the depth of the water. The deep water approximation (which is accurate to within 10% if the depth d is greater than one quarter of the wavelength) is used

$$\frac{\omega^2}{g} \approx \sqrt{k_w^2 + k_c^2}. \tag{4}$$

The temporal–angular spectrum is calculated as

$$S(\omega, \xi) = P(\omega)D(\xi). \tag{5}$$

A radial–Cartesian relationship between (ω, ξ) coordinates and (k_w, k_c) coordinates is defined by elementary geometry and (4). This allows the spectrum to be written as a function of k_w and k_c (note that scaling by the Jacobian of transformation is necessary as $S(\omega, \xi)$ is a density function).

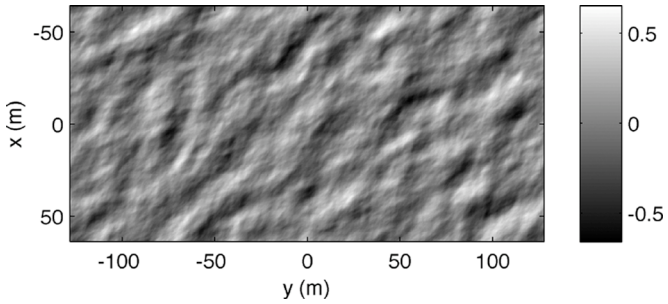

Fig. 2. Example of a simulated sea surface, with displacement plotted in meters.

Now that the spectrum has been defined on a rectangular spatial coordinate system, it can be readily employed in the computational generation of a sea-surface function. The square root of the spectral function $S(k_w, k_c)$ can be multiplied with 2-D complex Gaussian white noise (where the real and imaginary parts are zero-mean, unit-variance, and uncorrelated) to give amplitude and phase values for each (k_w, k_c) wave component; i.e., the product is used to define $a(k_w, k_c)$ and $\varphi(k_w, k_c)$ in the wave component

$$a(k_w, k_c)\sin\left(k_w\beta + k_c\gamma - \omega t + \varphi(k_w, k_c)\right) \tag{6}$$

where β is the windward spatial position, γ is the crosswind spatial position, and ω is defined by k_x and k_y as shown in (4). Summing all such components over k_w and k_c gives sea-surface height $h(\beta, \gamma, t)$. This function has a power spectrum consistent with the defined temporal spectrum (1), angular spectrum (2), and dispersion relation (4). The heights are also Gaussian distributed—a model which has previously been used in theoretical analysis [12]. A simple geometric rotation can be used to shift the windward–crosswind coordinate system to an arbitrarily oriented (x, y) system.

In Fig. 2, an example result from this type of simulation is shown. The surface displacement is plotted as a gray level as a function of space. The displacement of the spatial origin is shown as a function of time in Fig. 3. In this particular example, the wind speed is 6 m s^{-1}, the s parameter in the cos-2s spectrum is 11, and the wind direction is on a 45° angle from top-left to bottom-right. For these sea-state parameters, the Pierson–Moskowitz spectrum can be used to calculate a dominant temporal period of 4.4 s, a dominant wavelength of 30 m, and a displacement standard deviation of 0.19 m. All of these figures are consistent with the simulation shown.

The spectrum used here was constructed using common models of sea-surface statistics. Other statistical models of sea-surface parameters exist and could be incorporated into this method. For example, the Joint North Sea Wave Project (JONSWAP) spectrum [13] could be employed instead of the Pierson–Moskowitz model; there are also alternatives to the cos-2s distribution [14]; and the deep-water approximation need not be applied to the dispersion relation. The methods outlined in the rest of this paper could still be readily applied if such changes were to be made.

Authorized licensed use limited to: University of Illinois. Downloaded on August 5, 2009 at 17:03 from IEEE Xplore. Restrictions apply.

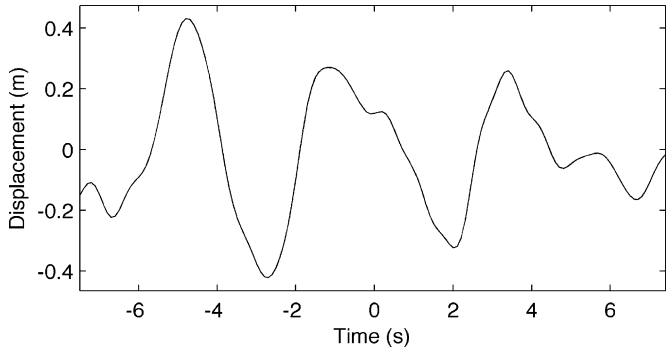

Fig. 3. Example of the displacement-versus-time plot for a single point in a simulated sea surface.

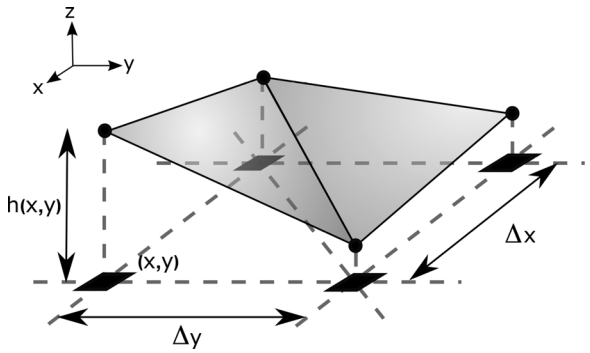

Fig. 4. Sea-surface displacement $h(x, y)$ is generated on a regular grid of (x, y) points and used to define triangular facets approximating the surface. Two triangular facets model the surface enclosed by four sample points.

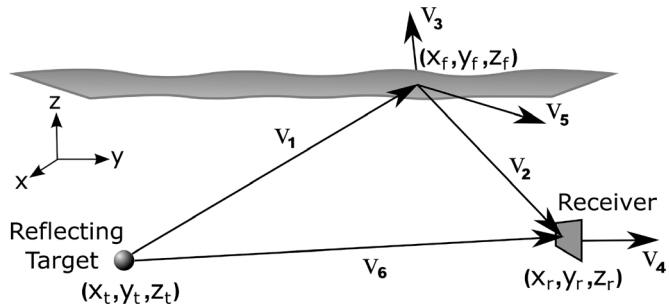

Fig. 5. Vectors used to calculate facet returns.

III. Faceted Sea-Surface Geometry

In order to calculate the multipath return from the sea surface, it is tiled into a contiguous set of reflecting facets. The easiest way to do this is to tile the surface into triangular surface elements—the three vertices of the triangle being defined by three (x, y, z) points. The aspect ratio is defined by the rectangular sampling grid with separation Δx and Δy. This tiling method is illustrated in Fig. 4.

The surface facet intercepts the scattered radiation from the target and reradiates some of it towards the receiver. The power density at the receiver is dependent on the area of the facet and various angles and distances related to the target, the facet, and the receiver. To facilitate the calculation of this power density, a vector system is defined as shown in Fig. 5.

The vector $\mathbf{v_1}$ is from the target to the facet of interest. The path from the facet to the receiver is $\mathbf{v_2}$, while $\mathbf{v_3}$ is the upward normal from the facet. The vector $\mathbf{v_4}$ is the receiver normal (pointing away from the imaged direction). The direction of specular reflection is given by $\mathbf{v_5}$ and $\mathbf{v_6}$ is the path from the target to the receiver.

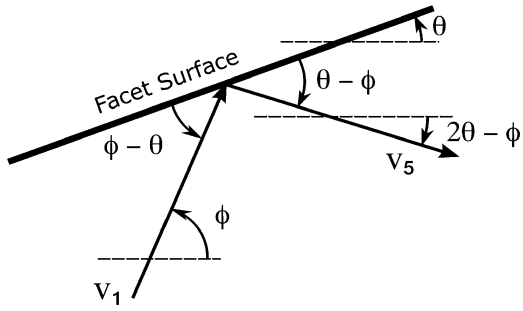

Fig. 6. Geometric relation used in the calculation of the reflected ray path.

If the horizontal position of the facet centroid (at time t) is given by x_f and y_f, then its height z_f can be defined as $z_f \equiv h(x_f, y_f, t)$. The vectors of Fig. 5 can then be defined as

$$\mathbf{v_1} = (x_f - x_t, y_f - y_t, z_f - z_t) \tag{7}$$
$$\mathbf{v_2} = (x_r - x_f, y_r - y_f, z_r - z_f) \tag{8}$$
$$\mathbf{v_3} = (-\tan\theta_x, -\tan\theta_y, 1) \tag{9}$$
$$\mathbf{v_4} = (0, 1, 0) \tag{10}$$
$$\mathbf{v_5} = \left(\frac{-1}{\tan(2\theta_x - \phi_x)}, \frac{-1}{\tan(2\theta_y - \phi_y)}, -1\right) \tag{11}$$
$$\mathbf{v_6} = (x_r - x_t, y_r - y_t, z_r - z_t). \tag{12}$$

In (10), it is assumed that the receiver is oriented parallel to the x-axis and pointing in the negative y direction. The angles θ_x, θ_y and ϕ_x, ϕ_y are the x and y values of facet-tilt angle and target-to-facet angle, respectively. The facet-tilt angles are easily calculated from the facet vertices and the target-to-facet angles are calculated from $\mathbf{v_1}$. These angles are used to calculate the reflected ray path $\mathbf{v_5}$. This reflection calculation is shown graphically in Fig. 6.

It should be noted that the ray angles can only be used to define the path of the reflection and not the direction. In (11), it is assumed that the z component is downward, however, this may not always be the case for steeply tilted facets. This problem can be resolved by checking the sign of the dot-product of $\mathbf{v_3}$ and $\mathbf{v_5}$—for a reflected ray it should be negative. If it is positive, (11) can be negated to reverse the direction.

IV. Determining the Scattering Strength of the Surface Facets

The vectors described in the previous section can now be used to calculate the contribution from each facet to the received multipath signal. The first step is to calculate the magnitude of the flux incident on the facet as

$$F(x_f, y_f) = \frac{1}{|\mathbf{v_6}|}\frac{1}{|\mathbf{v_1}|}\int_A \left\langle \frac{\mathbf{v_3}}{|\mathbf{v_3}|}, \frac{\mathbf{v_1}}{|\mathbf{v_1}|} \right\rangle dA$$
$$= \frac{1}{|\mathbf{v_6}|}\frac{1}{|\mathbf{v_1}|}\frac{|\mathbf{v_3}|}{\langle \mathbf{v_3}, \mathbf{z} \rangle}\iint_{xy} \left\langle \frac{\mathbf{v_3}}{|\mathbf{v_3}|}, \frac{\mathbf{v_1}}{|\mathbf{v_1}|} \right\rangle dxdy \tag{13}$$

Authorized licensed use limited to: University of Illinois. Downloaded on August 5, 2009 at 17:03 from IEEE Xplore. Restrictions apply.

where $\langle \cdot, \cdot \rangle$ represents the standard inner product, dA is the elemental area of the facet, and $\mathbf{z}$ is the unit vector in the z-direction. Without loss of generality, it has been assumed that the product of the broadcast power and the target reflectance is 1. Any beam-angle dependence of the radiation from the projector has been left out (this simply scales the multipath and direct responses and so can be included later, when modeling the SAS instrumentation) but the spreading losses from the transmitter to the target have been included. By making the assumption that the facets are small enough so that the vectors are approximately constant for any one facet, (13) can be rewritten as follows:

$$F(x_f, y_f) = \frac{1}{|\mathbf{v_6}|}\frac{1}{|\mathbf{v_1}|}\frac{|\mathbf{v_3}|}{\langle \mathbf{v_3}, \mathbf{z}\rangle}\frac{\Delta x \Delta y}{2}\left\langle \frac{\mathbf{v_3}}{|\mathbf{v_3}|}, \frac{\mathbf{v_1}}{|\mathbf{v_1}|}\right\rangle = \frac{\Delta x \Delta y}{2}\frac{\langle \mathbf{v_1}, \mathbf{v_3}\rangle}{|\mathbf{v_1}|^2\langle \mathbf{v_3}, \mathbf{z}\rangle|\mathbf{v_6}|}. \tag{14}$$

The flux received from the facet (or the facet "gain") can be calculated as

$$G(x_f, y_f) = \kappa F(x_f, y_f)\frac{1}{|\mathbf{v}_2|}\int_B \left\langle \frac{\mathbf{v_2}}{|\mathbf{v_2}|}, \frac{\mathbf{v_4}}{|\mathbf{v_4}|}\right\rangle dB = \kappa\frac{\Delta x \Delta y}{2}\frac{\langle \mathbf{v_1}, \mathbf{v_3}\rangle\langle \mathbf{v_2}, \mathbf{v_4}\rangle}{|\mathbf{v_1}|^2|\mathbf{v_2}|^2\langle \mathbf{v_3}, \mathbf{z}\rangle|\mathbf{v_4}||\mathbf{v_6}|} \tag{15}$$

where dB is the elemental area of the receiver. The complex factor κ describes the effect of the scattering from the facet. It is assumed that the surface area of the receiving hydrophone is small enough to consider the flux to be constant over the surface (which is normalized to an area of 1). The detection pattern of the receiver has been omitted but it would be a simple modification to include one if required. Also neglected is any time-varying gain factor which is often incorporated into physical implementations of pulse-echo sonar.

When using (15) to calculate the facet gain, there are certain nonphysical conditions under which the gain should be set to zero. These conditions are as follows:

1) if

$$\langle \mathbf{v_1}, \mathbf{v_3}\rangle < 0 \tag{16}$$

the path from the target to the facet penetrates the surface;

2) if

$$\langle \mathbf{v_2}, \mathbf{v_3}\rangle > 0 \tag{17}$$

the path from the facet to the receiver penetrates the surface;

3) if

$$\langle \mathbf{v_2}, \mathbf{v_4}\rangle < 0 \tag{18}$$

the facet is behind the receiver.

In Sections IV-A and IV-B, two methods will be outlined for calculating κ. Once this has been done and (15) evaluated, each facet will have a complex gain associated with it. Additionally, each facet will be assigned a delay time based on the time-of-flight calculation

$$\tau(x_f, y_f) = \frac{|\mathbf{v_1}| + |\mathbf{v_2}| - |\mathbf{v_6}|}{c} \tag{19}$$

where $\tau(x_f, y_f)$ gives the delay between the line-of-sight return and the multipath return from the facet. The speed of sound in water is c.

This simple model ignores any frequency-dependent behavior of the scattered field. Since SAS waveforms typically have a broad bandwidth, using this approach implies a simplification. The effects of a broad spectrum could be modeled by calculating κ for many frequencies in order to get transfer function for each facet. Rather than employing this more complicated approach (which also requires choosing a waveform), this paper shows analysis of an intuitive gain-and-delay model where each facet gives a displaced and scaled version of the signal reflected from the target. Therefore, the multipath returns are unaffected by sea-surface-induced dispersion, and as a result, are matched to the detection filter. This scenario represents a maximal clutter situation.

Sections IV-A and IV-B complete the simulation model by specifying the scattering coefficient κ. The scattering of waves from rough surfaces is a well-explored topic [15]–[18] and a number of approximate models for the phenomenon exist. Additionally, a significant amount of effort has been spent comparing scattering models and modeling the accuracy achieved, e.g., [19]–[25]. In this work, two relatively simple and computationally inexpensive scattering models will be used. These two models are described in Sections IV-A and IV-B.

A. Lambertian Scattering Model

The Lambertian model [26], [27] is a popular approach applicable when the surface is rough compared with a wavelength. Lambertian scattering is also known as perfectly diffused scattering, as the scattered field is broadly distributed and independent of the ensonification angle. This model is based on intensity rather than amplitude and since an amplitude-based model is required here, a few modifications to the basic form are needed.

If a field of intensity 1 is incident on a Lambertian surface with 100% reflectivity (the large index mismatch between water and air makes this an excellent approximation), the distribution of the reflected energy I, with respect to angle is

$$I(\vartheta) = \frac{\cos\vartheta}{\pi}. \tag{20}$$

The angle ϑ is between the outgoing ray path and the surface normal. The factor of $1/\pi$ ensures that energy is conserved. Spreading losses have been removed from this equation as they are already accounted for in (15). Taking the square root of (20) results in an expression for the modulus of the facet scattering coefficient

$$|\kappa| = \sqrt{\frac{1}{\pi}}\sqrt{\cos\vartheta} = \sqrt{\frac{1}{\pi}}\sqrt{\frac{\langle \mathbf{v_2}, -\mathbf{v_3}\rangle}{|\mathbf{v_2}||\mathbf{v_3}|}}. \tag{21}$$

Authorized licensed use limited to: University of Illinois. Downloaded on August 5, 2009 at 17:03 from IEEE Xplore. Restrictions apply.

As can be seen in (21), the factor $\cos\vartheta$ is easily expressed in terms of the vector system developed (as $\langle \mathbf{v_2}, -\mathbf{v_3}\rangle = |\mathbf{v_2}||\mathbf{v_3}|\cos\vartheta$).

Combining (15) and (21) gives an expression for the modulus of the Lambertian facet gain

$$|G_L(x_f, y_f)| = \frac{\Delta x \Delta y}{2\sqrt{\pi}} \frac{\langle \mathbf{v_1}, \mathbf{v_3}\rangle \langle \mathbf{v_2}, \mathbf{v_4}\rangle \sqrt{\langle \mathbf{v_2}, -\mathbf{v_3}\rangle}}{|\mathbf{v_1}|^2 |\mathbf{v_2}|^{2.5} \langle \mathbf{v_3}, \mathbf{z}\rangle \sqrt{|\mathbf{v_3}||\mathbf{v_4}||\mathbf{v_6}|}}. \tag{22}$$

Due to the rough nature of the surface under Lambertian scattering conditions, the phase of $G_L(x_f, y_f)$ is not predictable and is assigned a value between $-\pi$ and π randomly. Note that this Lambertian model is not frequency dependent and is thus valid across a broadband pulse.

B. Diffraction-Based Scattering Model

The model presented in this section is applicable when the sea surface spanned by a facet can be considered smooth on the scale of a wavelength. In this case, a specular reflection is dominant and a diffraction-based model is used to give κ, the angular pattern of this reflection. Each facet is considered as a separate aperture ensonified by the reflection from the target. Again, the contribution from each facet is calculated and the results summed to give the field at the receiver.

Let λ be the wavelength used and $H(\cdot,\cdot)$ be the 2-D Fourier transform of the unit function over the triangular facet. By applying the Kirchhoff approximation [16], [17] for each facet, Fourier optics [28] can be used to calculate the reflection pattern. The first step in performing this calculation is to define a coordinate system $\tilde{x}$, $\tilde{y}$, $\tilde{z}$ in which the facet surface lies in the $\tilde{x} - \tilde{y}$ plane. A vector in x, y, and z space can be rotated to $\tilde{x}$-, $\tilde{y}$-, $\tilde{z}$-axes by using the rotation matrix

$$\Phi = \begin{bmatrix} \cos\psi & \sin\psi\sin\theta_y & -\sin\psi\cos\theta_y \\ 0 & \cos\theta_y & \sin\theta_y \\ \sin\psi & -\cos\psi\sin\theta_y & \cos\psi\cos\theta_y \end{bmatrix}. \tag{23}$$

This matrix represents a rotation of θ_y about the x-axis followed by a rotation of ψ about the y-axis, where

$$\psi = \tan^{-1}(-\tan\theta_x \cos\theta_y). \tag{24}$$

Here θ_x and θ_y are the facet tilt angles illustrated in Fig. 6. In $\tilde{x}$, $\tilde{y}$, and $\tilde{z}$ space, the facet normal $\mathbf{v_3}$ lies along the $\tilde{z}$-axis and one facet edge runs along the $\tilde{y}$-axis. Unless the sea surface is completely flat, the triangle defined by the facet edges is not right-angled. However, the surface displacements are small compared with the lateral scale so it is only a small approximation to say the facet edges run along the $\tilde{x}$- and $\tilde{y}$-axes. The Fourier transform of a right-triangle can be calculated analytically and with this approximation can be used for $H(\cdot,\cdot)$. Specifically

$$H(k_x, k_y) \approx \frac{i\Delta y}{k_x}\left[\exp\left(-i\frac{k_x\Delta x}{2}\right)\operatorname{sinc}\left(\frac{k_y\Delta y}{2}\right) - \operatorname{sinc}\left(\frac{(k_x\Delta x + k_y\Delta y)}{2}\right)\right] \tag{25}$$

where $\operatorname{sinc}(k_y) = \sin(k_y)/k_y$. Note that for $k_x = 0$ it can be shown that the Fourier transform described is finite and continuous, and can be found from (25) using arguments based on the symmetry of the triangle function.

It should be noted that there are four possible facet orientations—the hypotenuse of the triangle can have either a positive or negative gradient in the $x - y$ plane and each hypotenuse is used in two differently oriented facets (as seen in Fig. 4). While the facet orientation has no impact in the Lambertian calculation, it does in this diffraction-based model as $H(\cdot,\cdot)$ varies with orientation. Simple Fourier transform properties can be used to calculate the transform of all four orientations from the Fourier transform of a single orientation. The simulations in this paper all consider a positive-gradient hypotenuse, as shown in Fig. 4. The expression given in (25) is the Fourier transform for the orientation of the leftmost facet seen in Fig. 4, projected onto the $x - y$ plane and with the origin positioned halfway along the hypotenuse.

Applying the transformation Φ to the vectors $\mathbf{v_2}$ and $\mathbf{v_5}$ gives $\tilde{\mathbf{v}}_\mathbf{2}$ and $\tilde{\mathbf{v}}_\mathbf{5}$, the path to the receiver, and the specular reflection path in $\tilde{x}$, $\tilde{y}$, and $\tilde{z}$ coordinates. These two vectors are normalized as

$$\frac{\tilde{\mathbf{v}}_\mathbf{2}}{|\tilde{\mathbf{v}}_\mathbf{2}|} = (\rho_{\tilde{x}}, \rho_{\tilde{y}}, \rho_{\tilde{z}}) \tag{26}$$

$$\frac{\tilde{\mathbf{v}}_5}{|\tilde{\mathbf{v}}_5|} = (\mu_{\tilde{x}}, \mu_{\tilde{y}}, \mu_{\tilde{z}}). \tag{27}$$

From these expressions, the scattering coefficient κ can be found

$$\kappa = \frac{-i}{\lambda}\frac{2\langle \mathbf{v_3}, \mathbf{z}\rangle}{\Delta x \Delta y |\mathbf{v_3}|}\sqrt{\frac{\langle \mathbf{v_2}, -\mathbf{v_3}\rangle}{|\mathbf{v_2}||\mathbf{v_3}|}} \times H\left(\frac{2\pi(\rho_{\tilde{x}} - \mu_{\tilde{x}})}{\lambda}, \frac{2\pi(\rho_{\tilde{y}} - \mu_{\tilde{y}})}{\lambda}\right). \tag{28}$$

This expression comes directly from the Fraunhofer far-field diffraction formula [28] but with some changes in appearance. The standard phase factor is accounted for by the delay $\tau(x_f, y_f)$ associated with each facet and the spreading losses are accounted for in (15). The κ factor is normalized by the facet area to be compatible with (15), which was determined in terms of flux through the facet rather than field strength. Additionally, the arguments of $H(\cdot,\cdot)$ are offset by μ terms. This arises from the oblique incidence of the arriving sound. It also gives the intuitive result that the reflected sound is at a maximum [i.e., $\kappa \propto H(0,0)$] along the specular reflection path. The same $\sqrt{\cos\vartheta}$ obliquity factor as used in the Lambertian model is included. Again, κ is written in terms of the vectors that have been defined for this problem.

The obliquity factor is often ignored when Fraunhofer diffraction patterns are calculated. It is important to include it in the analysis here, as results for large observation angles are calculated, i.e., the paraxial approximation violated. This does raise some doubt as to the validity of a Fraunhofer diffraction model, however the goal here is simply to get a physically justifiable beam-spread pattern from the facet. The obliquity factor ensures that when the reflected intensity is integrated over all observation angles the result is 1. That is, energy is conserved at the facet reflection. The dimensions of the facet determine the spread of the reflected sound around the specular reflection path—a large facet (which indicates the surface is smooth on a large spatial scale) gives a reflection that follows the specular reflection tightly, while a small facet gives a broad spread. The

Authorized licensed use limited to: University of Illinois. Downloaded on August 5, 2009 at 17:03 from IEEE Xplore. Restrictions apply.

scattering of the Lambertian model represents the limiting case of an infinitely small diffractive facet but with randomized scattered phase.

Substituting (28) into (15) results in the following expression for the facet gain in the diffraction-based model:

$$G_D(x_f, y_f) = H\left(\frac{2\pi(\rho_{\tilde{x}} - \mu_{\tilde{x}})}{\lambda}, \frac{2\pi(\rho_{\tilde{y}} - \mu_{\tilde{y}})}{\lambda}\right) \times \frac{-i\langle \mathbf{v_1}, \mathbf{v_3}\rangle\langle \mathbf{v_2}, \mathbf{v_4}\rangle\sqrt{\langle \mathbf{v_2}, -\mathbf{v_3}\rangle}}{\lambda|\mathbf{v_1}|^2|\mathbf{v_2}|^{2.5}|\mathbf{v_3}|^{1.5}|\mathbf{v_4}||\mathbf{v_6}|}. \quad (29)$$

This equation shows that the facet spread pattern is dependent on λ, and therefore, on the frequency of sound used. A more complete model could include a frequency-dependent spread pattern for broadband signals but here it is assumed that the facet transfer function is adequately modeled using the presented gain-and-delay approach.

C. Simulation Results

In this section, the functions $|G_L(x_f, y_f)|$ and $|G_D(x_f, y_f)|$ are plotted as a function of sea-surface position. These images represent the spatial distribution of the multipath contributions to the received signal. A transmitted frequency of $f_0 = 30$ kHz is simulated, the target is located at $(x_t, y_t, z_t) = (0, -50, -10)$ m, and the receiver is located at $(x_r, y_r, z_r) = (0, 50, -10)$ m. The sea surface from Fig. 2 is used in the simulations, as is the limiting case of a "flat" sea surface. The spacing between sample points is one half meter in both directions (i.e., $\Delta x = \Delta y = 0.5$ m). The flat surface is considered perfectly smooth in the diffraction-based model but capillary waves are assumed to be present to drive the scattering in the Lambertian model.

$|G_L(x_f, y_f)|$ is plotted as a function of surface position in Fig. 7. Each pixel represents the return from the area between four sea-surface sample points. As can be seen in Fig. 4, this corresponds to the return from two facets which are opposing triangles. The square root of the summed square magnitudes of the two gains is calculated to produce the Lambertian plots, as the model consists of incoherent returns across the facets. It can be seen that a strong return comes from above the target and a weaker peak from above the receiver. This is due to the broad Lambertian scattering and the spreading losses (given by $|\mathbf{v_1}|^{-1}|\mathbf{v_2}|^{-1}$) being minimized near points directly above the target and the receiver. The directionality of the receiver accounts for the peak above the target being stronger than the peak above the receiver.

The multipath contribution is plotted as a function of position for the diffraction-based model in Fig. 8. In this case, the gains of the two facets at each pixel are added before the magnitude is taken. This is because the diffraction-based model is a coherent model—the phase between facets is nonrandom. It can be seen that the contributions are much more localized in this case and, as expected, behave more like a specular reflection model.

The presence of capillary waves in the Lambertian model and the absence of capillary waves in the diffraction model is consistent with the fact that the facet size represents the largest area that can be reasonably approximated as flat in the sea surface. These differences explain the visible distinctions in Figs. 7 and 8. As mentioned in Section IV-B, the facet size can be varied

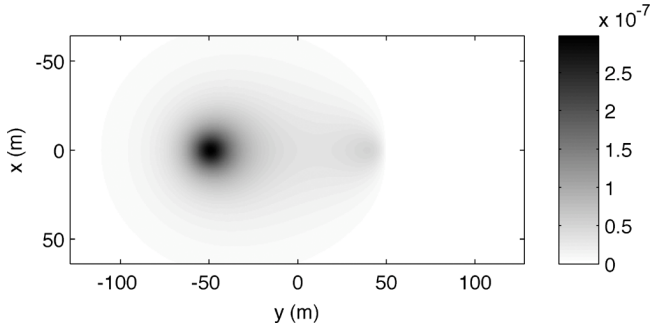

Fig. 7. Multipath return strength per facet pair (in units normalized by the line-of-sight return) as a function of position for a "flat" surface with capillary waves present, as required for the Lambertian model.

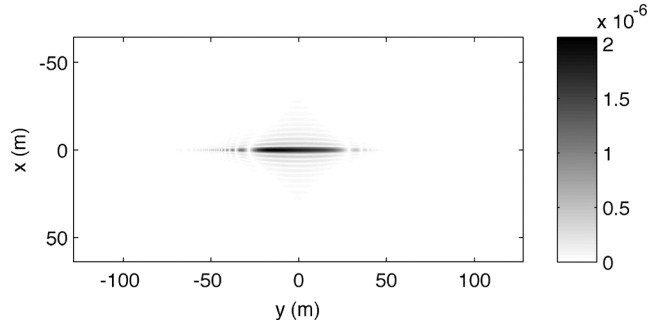

Fig. 8. Multipath return strength per facet pair (in units normalized by the line-of-sight return) as a function of position for a perfectly flat surface (no capillary waves present), as required for the diffraction model.

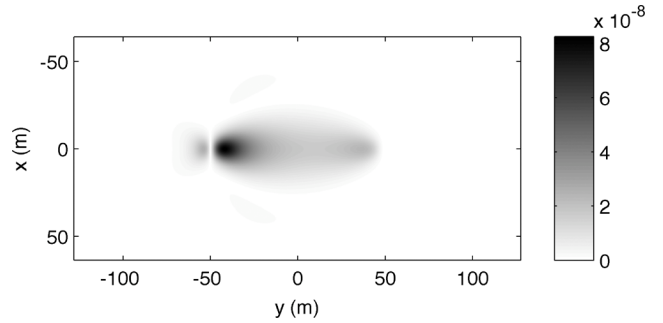

Fig. 9. Multipath return strength per facet pair (in units normalized by the line-of-sight return) as a function of position for a flat surface with the diffraction-based model and a smaller facet size.

to influence the spread from each facet. In Fig. 9, the diffraction-based results for a smaller facet size of $\Delta x = \Delta y = 0.05$ m are shown. In this case, the facet size is equal to the assumed wavelength and the spreading becomes broad. As expected, the sea-surface response looks more like the Lambertian case with broadly spread contributions. Note that the example of Fig. 9 contains a higher density of facets due to the finer discretization of the surface and so the amplitudes are not directly comparable to those shown in Figs. 7 and 8.

The differences between Figs. 8 and 9 illustrate how the facet size acts as a tunable parameter in the diffraction-based model. A larger facet size can be used for a smoother surface and results in a scattering model closer to specular reflection, while a smaller facet must be used for a rougher surface and gives a broader spread of energy. Regardless of the parameter

Authorized licensed use limited to: University of Illinois. Downloaded on August 5, 2009 at 17:03 from IEEE Xplore. Restrictions apply.

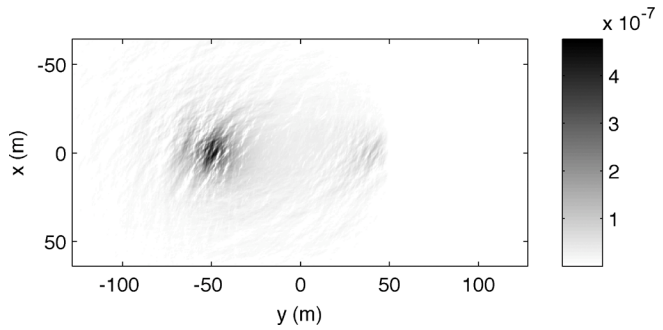

Fig. 10. Multipath return strength per facet pair (in units normalized by the line-of-sight return) as a function of position for a sea surface with the Lambertian model.

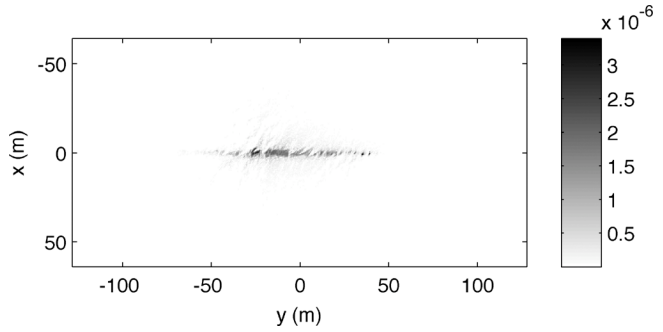

Fig. 11. Multipath return strength per facet pair (in units normalized by the line-of-sight return) as a function of position for a sea surface with the diffraction-based model.

size, phase coherence is maintained at surface reflection in the diffraction-based model. The Lambertian model gives a limiting case of a surface that is sufficiently finely structured to give very broad scattering and a complete loss of phase coherence at reflection. In the remaining simulations, both diffraction-based and Lambertian models will be investigated. A facet size of $\Delta x = \Delta y = 0.5$ m will be used as it is sufficiently small to both capture the structure of the sea surface and give a strong specular reflection in the diffraction-based model (as illustrated in Fig. 8).

When the surface has nonzero waveheight, some interesting behavior is revealed. The example sea surface from Fig. 2 is used to calculate the Lambertian response of Fig. 10. The same general trend as observed in Fig. 7 is seen but with the wave structure imposing areas of minimal or zero gain (and also increasing the maximum gain observed). These effects are due to sensitivity to facet angle. This is particularly pronounced when the inner-product checks of (16)–(18) are invoked to set a facet gain to zero. This occurs when a path from the target to the underside of the facet to the receiver does not exist.

The diffraction-based multipath image is plotted for the sea-surface realization in Fig. 11. It resembles its flat-surface counterpart but does have significant additional structure attributable to the surface waves. Like the Lambertian case, the tilts of the facets have the effect of reducing the gain in certain places and increasing it in others.

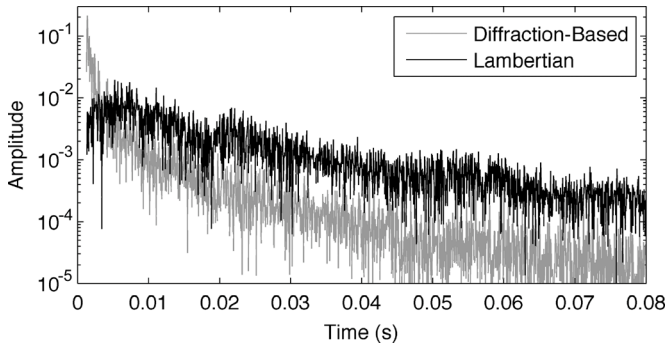

Fig. 12. Modulus of the impulse response for a sea surface with Lambertian and diffraction-based scattering models.

V. Determining the Impulse Response of a Target

Let $e(\tau)$ be the multipath echoes measured from the target when an impulse is transmitted and where τ is the delay time after the line-of-sight return arrives. For computational purposes, it is desirable to have $e(\tau)$ specified on a regularly sampled time scale—this means that the facet returns have to be binned into time slots. The set of facets in a given time bin $\mathcal{T}_n$ can be defined as

$$\mathcal{T}_n = \{(x_f, y_f) : (n-0.5)\Delta\tau \le \tau(x_f, y_f) < (n+0.5)\Delta\tau\}. \tag{30}$$

Here $\Delta\tau$ is the temporal sampling period of $e(\tau)$ and n indexes the temporal sample points. The sampling period is determined by the bandwidth of the sonar. Since assigning each facet to a given temporal sample point involves a small rounding of the associated delay, a phase factor is included in the facet gain to account for the small shift in effective delay. The value of the impulse response at a given time sample is simply the coherent sum of all the facet gains in that $\Delta\tau$-width bin

$$e[n] = \sum_{(x_f,y_f)\in\mathcal{T}_n} G(x_f, y_f) e^{-i\frac{2\pi c}{\lambda}[\tau(x_f,y_f) - n\Delta\tau]}. \tag{31}$$

Note that the discrete impulse response $e[n]$ is a weighted impulse train defined to approximate the effect of a system with impulse response $e(\tau)$.

Example impulse response amplitudes are shown in Fig. 12. These responses were calculated from the sea surface of Fig. 2, with a target located at (0, −50, −10) m and a receiver located at (0, 50, −10) m. The plots have been normalized so that the line-of-sight return would have an amplitude of 1.

A comparison between the Lambertian and diffraction-based impulse responses reveals some basic properties. Both responses have a set delay length of approximately 0.0012 s before multipath effects contribute, as there is a significant difference between the line-of-sight path length and the minimum multipath path length. Very soon after this delay gap both responses reach a maximum and then decay with time. The diffraction-based model tends to decay far more rapidly than the Lambertian model but has a similar root mean square (RMS) sum of multipath contributions. The phase of the impulse response is very rapidly varying (over a full 2π range) in both cases.

Authorized licensed use limited to: University of Illinois. Downloaded on August 5, 2009 at 17:03 from IEEE Xplore. Restrictions apply.

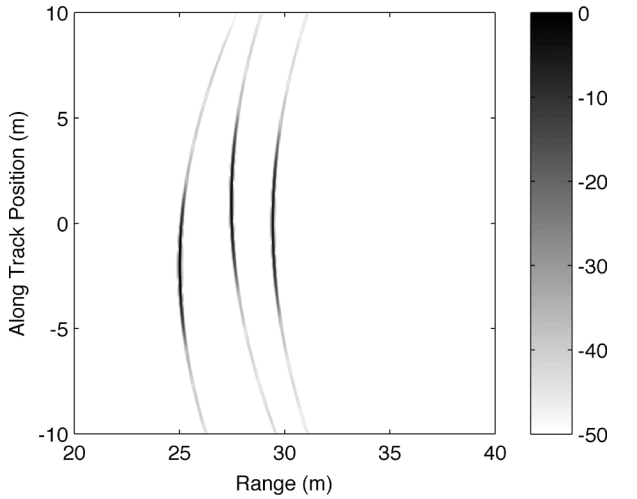

Fig. 13. Intensity (decibel scale) of the raw data for three point reflectors with no multipath effects.

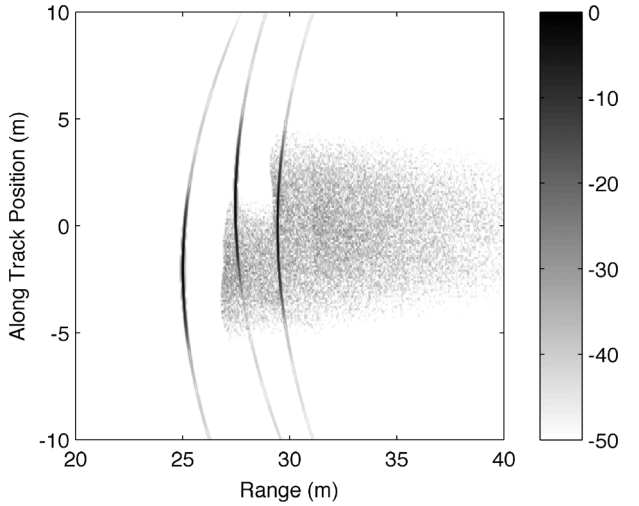

Fig. 14. Intensity (decibel scale) of the raw data for three point reflectors with multipath effects calculated using a Lambertian scattering model.

VI. SAS Imaging With Multipath Effects

Armed with the models developed up to this point, it is now possible to simulate the effects of multipath propagation in a SAS system. This process is shown by way of an example. First, it is necessary to specify certain operating parameters and approximations that are used.

It is assumed that there is no movement during the transmission and reception of a single pulse and that all movements of the surface and the sonar system occur in the time periods between the last echo return of one ping and the onset of transmission of the next ping. This is known as the "stop-and-hop" scenario. This does ignore any temporal Doppler effects that occur due to movement during a pulse. Existing SAS systems typically operate at maximum unambiguous ranges of less than 200 m and they mostly use a pulse repetition period shorter than 300 ms; consequently, the "stop-and-hop" scenario is believed to be accurate enough to model surface multipath effects.

The example SAS system considered operates at a central frequency of 30 kHz with a pulse bandwidth of 18 kHz. The transmitting and receiving apparatuses are assumed to be colocated 5 m below the sea surface and traveling in a straight 20-m path at a speed of 1 m s^{-1}. A pulse is transmitted every 0.1 s, resulting in 200 pings along the sonar path. The beam spread is determined by the length of the acoustic projector (22.5 cm) and the receiving hydrophone (33.5 cm).

A simulated object is defined with three equal-strength point scatterers located at a depth of 10 m. The sonar track is taken to be from $(x, y, z) = (-10, 0, -5)$ m to $(10, 0, -5)$ m, while the targets are located at $(-2, -24.5, -10)$ m, $(1, -27, -10)$ m, and $(0, -29, -10)$ m. A simulated sea surface is generated using the same parameters used to generate the surface seen in Fig. 2 and with spatial sampling periods of $\Delta x = \Delta y = 0.5$ m. Temporally, the surface evolves in 0.1-s time increments so that a multipath response can be generated for each ping. These multipath responses are incorporated into standard SAS modeling methods [1] to give simulated SAS data with multipath effects included.

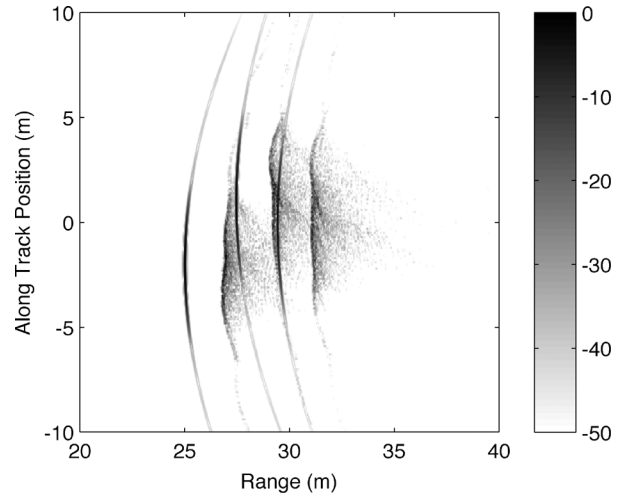

Fig. 15. Intensity (decibel scale) of the raw data for three point reflectors with multipath effects calculated using a diffraction-based scattering model.

Data without multipath effects are displayed in Fig. 13. The intensity (i.e., the square magnitude) of the data is displayed on a decibel scale so that low-level detail can be seen. Data with multipath effects can be seen in Fig. 14 (Lambertian scattering model) and Fig. 15 (diffraction-based scattering model).

The effects of the surface multipath are clearly seen in Figs. 14 and 15. In both cases, the multipath returns partially obscure line-of-sight data. It is easy to envision situations in which multipath returns from a strong target overwhelm the direct response from a more distant weak reflector. Additionally, in the diffraction-based model (which describes reflections of a specular nature), the multipath returns could be easily mistaken for line-of-sight returns.

SAS reconstruction algorithms [1] can now be applied to the data generated in order to get a synthetic aperture image. In this case, the wave-number algorithm is chosen. A reconstruction free of multipath effects is shown in Fig. 16. It can be seen that the point targets are well imaged. Reconstructions from the multipath data can be seen in Figs. 17 and 18. The multipath effects

Authorized licensed use limited to: University of Illinois. Downloaded on August 5, 2009 at 17:03 from IEEE Xplore. Restrictions apply.

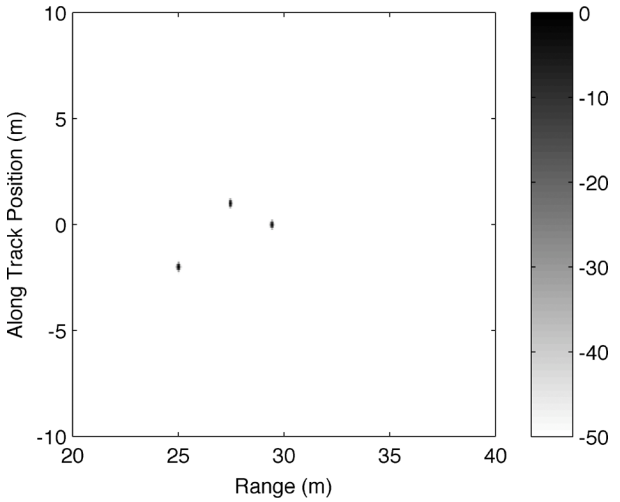

Fig. 16. Intensity (decibel scale) of the reconstructed SAS image with no multipath effects.

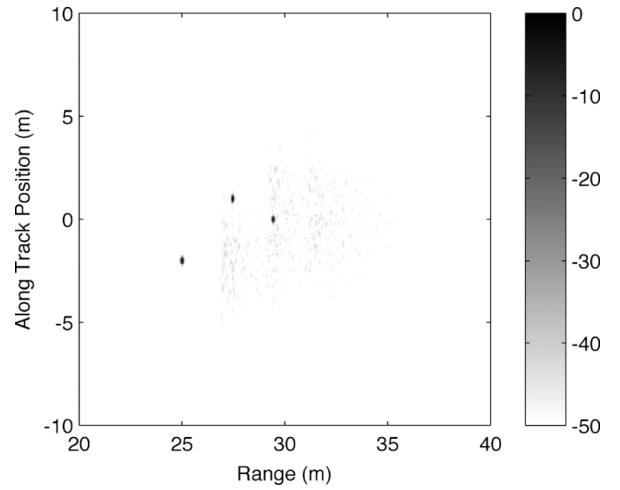

Fig. 17. Intensity (decibel scale) of the reconstructed SAS image with multipath effects calculated using a Lambertian scattering model.

in these images are arguably less pronounced than in the raw data. This effect is discussed further in the following section.

VII. Mitigation of Multipath Effects by SAS Processing

The simulation approach described here allows the separation of signal resulting from the desirable line-of-sight return and the clutter produced by multipath propagation. This allows a signal-to-clutter ratio (SCR) to be calculated, where the clutter is due solely to multipath propagation. The energy measure used in this calculation is the sum of the square magnitude of the signal.

The wave-number reconstruction algorithm is simply a resampling in Fourier space combined with a lowpass filter. This means that the energy in the line-of-sight and clutter signals changes only because of the lowpass filtering effect. Therefore, the SCR should change only slightly between the raw data and the SAS reconstruction if the total energy in the image is considered. This is confirmed by the results shown in Table I in the "Image SCR" columns. There is a slight increase in SCR in the SAS reconstructions that can be attributed to the clutter having more energy in the high-frequency regions attenuated by the lowpass filter in the wave-number algorithm.

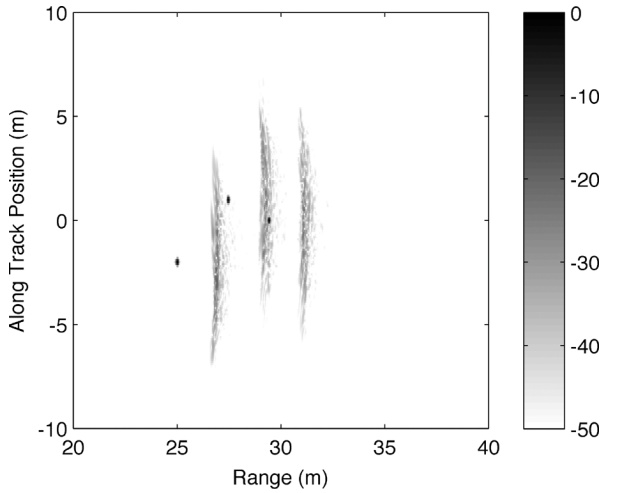

Fig. 18. Intensity (decibel scale) of the reconstructed SAS image with multipath effects calculated using a diffraction-based scattering model.

TABLE I
Signal to Multipath-Clutter Ratios in the Example Data

	Image SCR (dB)		Line SCR (dB)	
	Lambertian	Diffraction	Lambertian	Diffraction
Raw Data	15.8	4.94	15.6	4.70
SAS Image	17.4	6.40	30.1	20.5

However, Figs. 14–17 show that SAS reconstruction techniques appear to lessen the effect of the clutter signal. This is because the reconstruction algorithm moves the line-of-sight signal to the correct localized position (with an associated gain in intensity), while leaving the multipath contributions at a lower level and distributed over a wide spatial range. The multipath signals do not have the spatial phase relation required to give a localized signal after SAS processing. This effect can be quantified by using a "line SCR," which is the SCR along a single cross-track range line with an along-track coordinate that matches the position of one of the targets. Data from only one target is used to calculate this figure, which is displayed in Table I for the target closest to the SAS towfish in the previous simulations. The along-track localization of the line-of-sight signal combined with the lack of localization of the multipath clutter in the SAS reconstructions results in a significant line SCR improvement over the raw data.

The results shown in Table I indicate that specular reflections to the receiver result in a significantly poorer SCR if the sea surface is smooth enough to be well modeled by the diffraction-based model. Indeed, in the raw data, the diffraction-based multipath returns have a spatial distribution similar to that produced by the line-of-sight signal. This indicates that in conventional sonar systems the diffraction-based multipath return may be mistaken for a second, more distant, target. The surface roughness inherent in the Lambertian model significantly broadens the spread of the multipath clutter and thus lessens its effect. SAS processing improves the clutter performance in both cases as the line-of-sight signal is localized to a single along-track location while the multipath clutter remains spatially disperse. It should be noted that in crowded scenes the multipath clutter from different targets may overlap, resulting

Authorized licensed use limited to: University of Illinois. Downloaded on August 5, 2009 at 17:03 from IEEE Xplore. Restrictions apply.

in an increase of the effective clutter level that would not be captured by the single-target line SCR analysis presented here. That is, as the density of targets increases, the improvement in line SCR provided by synthetic aperture processing decreases.

If a target returns signal over an effective width of p pings, then the coherent sum over these p pings should give a SAS reconstruction intensity that is proportional to p^2. Assuming that the multipath returns are also present over the p pings and that they sum incoherently in the SAS reconstruction, the average multipath intensity in the SAS reconstruction should be proportional to p. The line SCR between the raw and SAS data can then be expected to increase by $10\log(p^2/p)$. In the simulations presented in the previous section, the signal amplitudes decay to half of their maximums at approximately $p = 35$, giving an expected increase in line SCR of 15.4 dB. This is consistent with the line SCR figures seen in Table I. The consistency between an incoherent-multipath model and the improvement in line SCR is certainly expected for the Lambertian model, where the randomized phase introduced at reflection guarantees an incoherent multipath response. However, the diffraction-based model preserves phase at reflection, and therefore, there is a possibility of ping-to-ping correlations. That the line SCR improves in a manner consistent with an incoherent-multipath model indicates that these correlations are either small or at least do not result in a more localized response after synthetic aperture processing.

The simulation method presented here gives a means for investigating the expected effects of multipath propagation for a given SAS system, sea state, and target configuration. While the number of parameters present in this description is too large to present an exhaustive characterization of multipath effects, an example study can be seen in Fig. 19. These simulations have the same system parameters as those presented in Section VI except that the wind speed is varied and only the target nearest to the SAS towfish is considered. Multiple realizations of the sea surface are used at each wind speed and Fig. 19 shows the resulting average line SCRs and their variability.

The diffraction-based results shown in Fig. 19 show an increase in SCR as wind speed increases from zero and disturbs the sea surface. It can also be seen that the Lambertian-based results are not strongly affected by wind speed. The variability of the diffraction-based SCR is high since the clutter strength depends strongly on whether a specular reflection happens to point toward the receiver. However, the summation inherent in synthetic aperture processing does reduce the variability of the diffraction-based SAS SCR. As expected, the broadly scattering Lambertian model shows less variability across realizations of the sea surface. At all wind speeds, the SCR improvement between the SAS and raw cases remains relatively constant. This indicates that for the system parameters investigated here, the multipath returns tend to add incoherently in the SAS data at all wind speeds.

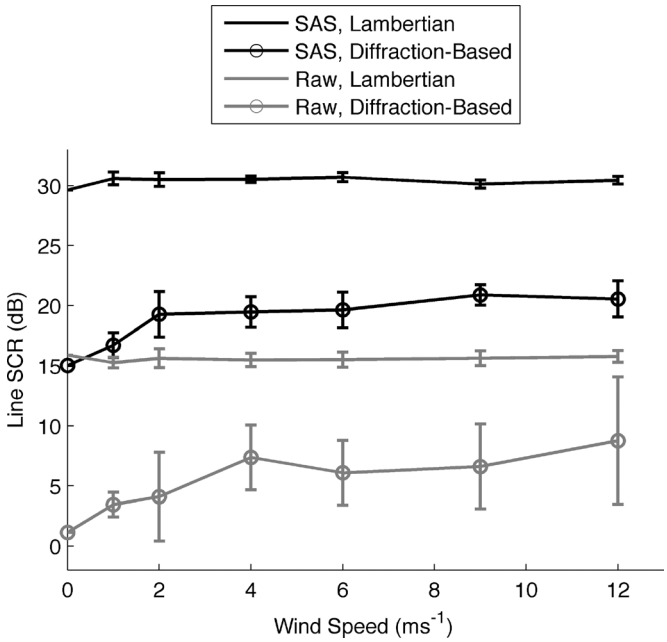

Fig. 19. Line SCR as a function of wind speed. Ten realizations of the sea surface were used at each wind speed and the average SCR is plotted with error bars indicating the standard deviation at each point.

VIII. Conclusion

A stochastic, physics-based model for surface multipath contributions to sonar data has been presented. This model uses the Pierson–Moskowitz spectrum to model the sea-surface statistics, and Lambertian and diffraction-based models for the cases of rough-surface (i.e., with capillary waves present) and smooth-surface scattering, respectively. The calculated multipath contributions were used to generate simulated sonar data. These data were used to show that while SAS systems correctly localize the line-of-sight signal returned from a target, the multipath returns are not similarly localized as they do not have the correct interping phase relation. Thus, when compared to raw data (as displayed in conventional sonar), the SAS reconstructions have stronger, more localized target estimates but the multipath contributions remain spatially broad. Thus, SAS processing improves the effective signal-to-multipath-clutter ratio. Simulations suggest that this effect may be quantified by modeling the line-of-sight signal as coherent from ping to ping and the multipath clutter as incoherent.

The developed model employs a number of assumptions but the simulation framework may still be used under differing system conditions. For example, the Lambertian and diffraction-based scattering models are applicable in certain sea-surface conditions but could be replaced by alternative scattering models for different surface conditions. Similarly, each facet is modeled as a delay-and-gain element but a dispersive scattering model can be employed at the cost of additional computational effort. One may also include the rate of sea-surface change to model Doppler effects, or the continuous movement of the towfish to remove the stop-and-hop assumption. It should be noted that modifying the model to remove the gain-and-delay and/or Doppler-free assumptions can be expected to improve the SCR as the multipath waveform will no longer be perfectly matched to the detector. However, there are other effects which are not well modeled in the framework provided, e.g., strong multipath returns may adversely affect the performance of SAS micronavigation systems, which will in turn affect image quality.

Authorized licensed use limited to: University of Illinois. Downloaded on August 5, 2009 at 17:03 from IEEE Xplore. Restrictions apply.

REFERENCES

[1] P. T. Gough and D. W. Hawkins, "Unified framework for modern synthetic aperture imaging systems," *Int. J. Imag. Syst. Technol.*, vol. 17, no. 8, pp. 343–358, 1997.

[2] J. T. Christoff, "Motion-compensated high frequency synthetic aperture sonar," *J. Acoust. Soc. Amer.*, vol. 103, no. 5, p. 2950, 1998.

[3] P. T. Gough and M. A. Miller, "Displaced ping imaging autofocus for a multi-hydrophone SAS," *Inst. Electr. Eng. Proc.—Radar Sonar Navig.*, vol. 151, no. 3, pp. 163–170, Jun. 2004.

[4] J. C. Novarini and J. W. Caruthers, "Numerical modeling of acoustic-wave scattering from randomly rough surfaces: An image model," *J. Acoust. Soc. Amer.*, vol. 53, no. 3, pp. 876–884, 1973.

[5] J. C. Novarini and H. Medwin, "Diffraction, reflection, and interference during near-grazing and near-normal ocean surface backscattering," *J. Acoust. Soc. Amer.*, vol. 64, no. 1, pp. 260–268, 1978.

[6] H. Medwin and J. C. Novarini, "Backscattering strength and the range dependence of sound scattered from the ocean surface," *J. Acoust. Soc. Amer.*, vol. 69, no. 1, pp. 108–111, 1981.

[7] W. A. Kinney, C. S. Clay, and G. A. Sandness, "Scattering from a corrugated surface: Comparison between experiment, Helmholtz-Kirchhoff theory, and the facet-ensemble method," *J. Acoust. Soc. Amer.*, vol. 73, no. 1, pp. 183–194, 1983.

[8] M. Pinto, A. Bellettini, L. S. Wang, P. Munk, V. Myers, and L. Pautet, "A new synthetic aperture sonar design with multipath mitigation," in *Proc. AIP Conf. High Frequency Ocean Acoust.*, 2004, vol. 728, pp. 489–496.

[9] W. J. Pierson and L. Moskowitz, "A proposed spectral form for fully developed wind seas based on the similarity theory of S.A. Kitaigorodskii," *J. Geophys. Res.*, vol. 69, pp. 5181–5190, 1964.

[10] R. B. Long, "The statistical evaluation of directional spectrum estimates derived from pitch/roll buoy data," *J. Phys. Ocean.*, vol. 10, pp. 944–952, 1980.

[11] H. Lamb, *Hydrodynamics*. New York: Dover, 1932, ch. 228, pp. 364–365.

[12] M. S. Longuet-Higgins, "On the statistical distribution of the wave heights of sea waves," *J. Mar. Res.*, vol. 11, pp. 245–266, 1952.

[13] K. Hasselmann, T. P. Barnett, E. Bouws, H. Carlson, D. E. Cartwright, K. Enke, J. A. Ewing, H. Gienapp, D. E. Hasselmann, P. Kruseman, A. Meerburg, P. Miller, D. J. Olbers, K. Richter, W. Sell, and H. Walden, "Measurements of wind-wave growth and swell decay during the north sea wave project (JONSWAP)," *Ergänzungsheft zur Deutschen Hydrographischen Zeitschrift Reihe*, vol. 8, pp. 1–95, 1973.

[14] A. Lygre and H. E. Krogstad, "Maximum entropy estimation of the directional distribution in ocean wave spectra," *J. Phys. Ocean.*, vol. 16, pp. 2052–2060, 1986.

[15] P. Beckmann and A. Spizzichino, *The Scattering of Electromagnetic Waves From Rough Surfaces*. Oxford, U.K.: Pergamon, 1963, Part I, pp. 1–214.

[16] L. M. Brekhovskikh and Y. P. Lysanov, *Fundamentals of Ocean Acoustics*, 3rd ed. New York: Springer-Verlag, 2003, ch. 9 and 10, pp. 183–249.

[17] J. A. Ogilvy, *Theory of Wave Scattering From Random Rough Surfaces*. Bristol, U.K.: Adam Hilger, 1991, ch. 1–4, pp. 1–117.

[18] L. Fortuin, "Survey of literature on reflection and scattering of sound waves at the sea surface," *J. Acoust. Soc. Amer.*, vol. 47, pp. 1209–1228, 1970.

[19] D. R. Jackson, D. P. Winebrenner, and A. Ishimaru, "Comparison of perturbation theories for rough-surface scattering," *J. Acoust. Soc. Amer.*, vol. 83, pp. 961–969, 1988.

[20] E. I. Thorsos, "The validity of the Kirchhoff approximation for rough surface scattering using a Gaussian roughness spectrum," *J. Acoust. Soc. Amer.*, vol. 83, pp. 78–92, 1988.

[21] E. I. Thorsos and D. R. Jackson, "The validity of the perturbation approximation for rough surface scattering using a Gaussian roughness spectrum," *J. Acoust. Soc. Amer.*, vol. 86, pp. 261–277, 1989.

[22] E. I. Thorsos, "Acoustic scattering from a "Pierson-Moskowitz" sea surface," *J. Acoust. Soc. Amer.*, vol. 88, pp. 335–349, 1990.

[23] P. J. Kaczkowski and E. I. Thorsos, "Application of the operator expansion method to scattering from one-dimensional moderately rough Dirichlet random surfaces," *J. Acoust. Soc. Amer.*, vol. 96, pp. 957–972, 1994.

[24] E. I. Thorsos and S. L. Broschat, "An investigation of the small slope approximation for scattering from rough surfaces. Part I. Theory," *J. Acoust. Soc. Amer.*, vol. 97, pp. 2082–2093, 1995.

[25] S. L. Broschat and E. I. Thorsos, "An investigation of the small slope approximation for scattering from rough surfaces. Part II. Numerical studies," *J. Acoust. Soc. Amer.*, vol. 101, pp. 2615–2625, 1997.

[26] J. H. Lambert, *Photometria Sive de Mensura et Gradibus Luminis, Colorum et Umbrae*. Augsburg, Germany: Eberhard Klett, 1760.

[27] B. K. P. Horn and R. W. Sjoberg, "Calculating the reflectance map," *Appl. Opt.*, vol. 18, pp. 1770–1779, 1979.

[28] J. W. Goodman, *Introduction to Fourier Optics*, ser. Electrical and Computer Engineering: Electromagnetics, 3rd ed. Greenwood Village, CO: Roberts, 2004, ch. 4, pp. 63–96.

Brynmor J. Davis (S'04–M'06) received the B.E. degree in electrical and electronic engineering from the University of Canterbury, Christchurch, New Zealand, in 1999, the M.S. degree in electrical and computer engineering from the University of Arizona, Tucson, in 2001, and the Ph.D. degree in electrical and computer engineering from Boston University, Boston, MA, in 2006.

Currently, he is a Postdoctoral Research Associate at the Beckman Institute for Advanced Science and Technology, University of Illinois at Urbana-Champaign, Urbana. His research interests include inverse problems, optics and acoustics, statistical signal processing, coherence theory, microscopy, and remote sensing.

Peter T. Gough (SM'97) received the B.E. degree (with honors) and the Ph.D. degree from the University of Canterbury, Christchurch, New Zealand, in 1970 and 1975, respectively, both in electrical engineering .

From 1975 to 1978, he was with The Institute of Optics, University of Rochester, Rochester, NY, and from 1979 to 1980, he was with the Electrical Engineering Department, University of Manitoba, Winnipeg, MB, Canada. In 1981, he joined the Electrical Engineering Department, University of Canterbury, where he is now Full Professor. He was Head of that department from 1991 to 1995 and is a founding member of the Acoustic Research Group.

Dr. Gough is a Fellow of the Institute of Professional Engineers of New Zealand.

Bobby R. Hunt (S'66–M'67–SM'77–F'83–LF'07) received the B.Sc. degree in aeronautical engineering and electrical engineering from Wichita State University, Wichita, KS, in 1964, the M.Sc. degree in electrical engineering and mathematics from Oklahoma State University, Stillwater, in 1965, and the Ph.D. degree in systems engineering and electrical engineering from University of Arizona, Tucson, in 1967.

He was a staff member of the Los Alamos National Laboratory (1968–1975). He joined the Faculty of the University of Arizona in 1975 and held appointments, through 2001, in systems engineering, electrical engineering, optical sciences, and applied mathematics. In 1981, he joined the technical staff of Science Applications International Corporation and since 2001 he has held the position of Vice President, and served in that position as the Chief Scientist of the Maui High Performance Computing Center.

Dr. Hunt is a Fellow of the Optical Society of America.

Authorized licensed use limited to: University of Illinois. Downloaded on August 5, 2009 at 17:03 from IEEE Xplore. Restrictions apply.